Activity, Selectivity and Initial Degradation of Iron Molybdate in the Oxidative Dehydrogenation of Ethanol

Niklas Oefner,[a] Franziska Heck,[b] Marcel Dürl,[c] Leon Schumacher,[d] Humera Khatoon Siddiqui,[e] Ulrike I. Kramm,[e] Christian Hess,[d] Angela Möller,[c] Barbara Albert,[b] and Bastian J. M. Etzold*[a]

Iron molybdate catalysts are applied in the industrial *FormOx* process to produce formaldehyde by oxidative dehydrogenation (ODH) of methanol. Only few studies are available about the applicability of iron molybdate catalysts for the ODH of ethanol to produce acetaldehyde. Herein, an iron molybdate synthesized by co-precipitation (p) and an iron molybdate prepared by a ball-milling solid-state synthesis (bm) are applied as ethanol ODH catalysts. Both materials show attractive acetaldehyde selectivites of $>90\,\%$ (280 °C: p-$Fe_2(MoO_4)_3$: $Y_{AcH} = 90.3\,\%$; bm-$Fe_2(MoO_4)_3$: $Y_{AcH} = 60.4\,\%$) and a stable performance. The bulk composition and crystal structure could be confirmed by various characterization techniques and is maintained during ethanol ODH. XPS reveals an enrichment of Mo on the catalyst surface which is slightly decreasing after the catalytic tests. This observation could be a first sign of long-term deactivation like known from methanol ODH. Comparing the performance of both materials, p-$Fe_2(MoO_4)_3$ shows higher activity and aldehyde selectivity. We propose the higher Mo/Fe surface ratio and the lower acidity to be the reasons for these differences.

Introduction

In 2020, fossil resources like crude oil, natural gas and coal represented 85 % of feedstocks in the global carbon-based chemical industry.[1] For the aspired defossilization of the chemical industry it is indispensable to provide strategies in order to substitute these fossil resources. In such a circular economy, these substitutes can be either waste streams or renewable resources. A commodity that is already produced in large scale based on renewable resources is ethanol. In 2019, 109 billion liters of ethanol were globally produced from sugar or starch containing resources like corn, sugar cane and sugar beets, and the production is predicted to increase to 130 billion liters in 2024.[2,3] Besides the production of bioethanol from sugar containing raw materials, a second-generation bioethanol production is rising. These new techniques are able to convert cellulosic plant parts like straw or residues into so-called cellulosic ethanol.[4]

Most of the produced bioethanol is added to gasoline to produce biofuels but bioethanol is also used as a feedstock in the chemical industry. There are several plants, for example by Braskem, Chematur, British petroleum or Axens which produce ethylene by dehydration of bioethanol on an industrial scale.[4] The Braskem ethylene plant in Brazil, which started operation in 2010, produces 200 000 $t\,a^{-1}$. This so-called bioethylene is further used to produce bio-based polymers like polyethylene.

Besides ethylene, bioethanol can be used as a sustainable feedstock to produce other important platform chemicals like acetaldehyde, acetic acid, ethyl acetate, ETBE etc.[5] The selective oxidation of ethanol leads to acetaldehyde:

$$CH_3CH_2OH\,(g) + 0.5\,O_2\,(g) \rightarrow CH_3CHO\,(g) + H_2O\,(g)$$

$$\Delta_R H = -177\,kJ\,mol^{-1}$$

Today, acetaldehyde is produced by the Wacker-Hoechst process through oxidation of ethylene.[6] Here, ethylene is oxidized in aqueous solution at 100–130 °C using a $PdCl_2/CuCl_2$ catalyst.[6] The low reaction temperature in the Wacker-Hoechst process hinders efficient usage of the heat of reaction. In contrast, a gas-phase conversion like the ethanol ODH operating at higher temperatures would allow employing the heat of reaction more efficiently, leading to a decrease of the overall energy and CO_2 footprint of the process.[7] Besides this energetic aspect and the clear advantage of using bioethanol as a

[a] N. Oefner, Prof. B. J. M. Etzold
Ernst-Berl-Institut für Makromolekulare und Technische Chemie
Technische Universität Darmstadt
Alarich-Weiß-Straße 8, 64287 Darmstadt (Germany)
E-mail: bastian.etzold@tu-darmstadt.de
[b] F. Heck, Prof. B. Albert
Eduard-Zintl-Institut für Anorganische und Physikalische Chemie
Technische Universität Darmstadt
Alarich-Weiß-Straße 12, 64287 Darmstadt (Germany)
[c] M. Dürl, Prof. A. Möller
Department of Chemistry
Johannes Gutenberg-University Mainz
Duesbergweg 10–14, 55128 Mainz
(Germany)
[d] L. Schumacher, Prof. C. Hess
Eduard-Zintl-Institut für Anorganische und Physikalische Chemie
Technische Universität Darmstadt
Alarich-Weiß-Straße 12, 64287 Darmstadt (Germany)
[e] H. Khatoon Siddiqui, Prof. U. I. Kramm
Eduard-Zintl-Institut für Anorganische und Physikalische Chemie
Technische Universität Darmstadt
Alarich-Weiß-Straße 12, 64287 Darmstadt (Germany)

Supporting information for this article is available on the WWW under https://doi.org/10.1002/cctc.202101219

sustainable feedstock, the ODH of ethanol can be applied to many catalyst systems, preventing the usage of critical raw materials like palladium that is used in the Wacker-Hoechst process.

Due to this attractiveness, different catalyst systems have been studied for ethanol ODH. The main classes of investigated catalysts are supported metal oxides, mainly supported VO_x,[7–24] mixed metal oxides,[25,26] supported metal catalysts[27–30] or carbon-based catalysts.[31–33] Supported vanadium oxide catalysts show high activity in the ODH of ethanol. Activity and selectivity strongly depend on the nature of the support material, where the activity increases with increasing metal-support-interaction.[7,23] High acetaldehyde selectivity and a yield of around 90% could be reached with a VO_x/TiO_2 catalyst.[13] Besides supported metal oxides, supported metal catalysts, especially the coinage metals, have been investigated as ethanol dehydrogenation catalysts. For example, Liu *et al.* used gold nanoparticles supported on $(Mg,Cu)Cr_2O_4$ spinel as ethanol ODH catalyst with an acetaldehyde yield of 95%.[30]

Only few studies used mixed metal oxides as ethanol ODH catalysts. $MoVO_x$ catalysts, which are applied industrially in the oxidation of acrolein to acrylic acid, also show promising results in the selective oxidation of ethanol.[26] By doping $MoVO_x$ mixed oxides with tellurium, Sobolev *et al.* performed temperature programmed reactions with 2 vol% ethanol and 18 vol% oxygen on a $MoV_{0.3}Te_{0.2}O_x$ catalyst and reached nearly quantitative yield of acetaldehyde at 220 °C.[26]

Another mixed oxide system that is employed industrially on a large scale within the *FormOx* process is iron molybdate.[34–36] In this case, methanol is directly oxidized with oxygen to formaldehyde at temperatures between 260 and 400 °C.

$$CH_3OH\ (g) + 0.5\ O_2\ (g) \rightarrow CH_2O\ (g) + H_2O\ (g)$$

$$\Delta_R H = -147\ \mathrm{kJ\,mol^{-1}}$$

At nearly full conversion, the selectivity to formaldehyde still exceeds 90%, leading to overall plant yields of 88–91%.[34] Besides the attractive activity and selectivity of iron molybdates in methanol ODH, the catalytic system suffers from deactivation through molybdenum depletion. Under reaction conditions, volatile molybdenum-oxy-methoxy or molybdenum-oxy-hydroxy species are formed and sublimated from the surface leaving behind a molybdenum depleted catalyst.[37–40] These volatile species decompose in colder zones of the reactor and deposit between the catalyst pellets, blocking the reactor and causing increased pressure drops.[41]

Nevertheless, iron molybdate catalysts show great performance in methanol ODH and are available on large scale. Concerning the applicability of iron molybdates as catalysts for the ethanol ODH reaction only few studies are available.[42–45] These studies had either a different intention (e.g. application in planar ethanol sensors;[42] direct 1,1-diethoxyethane production[44]) or operated at low degree of conversion (< 30%) and time on streams[45] or at very high temperatures (350 °C)[43], thus making an assessment of the applicability of iron molybdate catalysts for ethanol ODH difficult.

In this work, the suitability of $Fe_2(MoO_4)_3$ as catalyst for ethanol ODH is studied. In addition to a classical precipitation-based synthesis route, iron molybdate stemming from a modified ball-milling solid-state synthesis is employed. The catalysts are benchmarked in methanol ODH, since a substantial amount of literature data is available for comparison. The activity, selectivity, and stability of the catalyst in ethanol ODH is investigated in detail. Extensive characterization prior and after catalysis is carried out, employing SEM-EDX, N_2-physisorption, ICP-OES, XRD, XPS, Raman and Mössbauer spectroscopy to investigate reaction-induced changes in structure and composition of the materials. Due to the strong interlink of characterization prior and after catalysis and catalytic performance itself, all results are presented first and afterwards the discussion is based on the full holistic picture.

Results

In the following sections, iron molybdate prepared by the classical co-precipitation method from iron nitrate and ammonium heptamolybdate is referred to as p-$Fe_2(MoO_4)_3$ and iron molybdate synthesized by ball-milling solid-state reaction from Fe_2O_3 and MoO_3 is labelled bm-$Fe_2(MoO_4)_3$. The material that was used for the ethanol ODH temperature cycling experiments is extensively characterized and labelled as "spent" material.

Ethanol ODH. Both iron molybdate catalysts were tested for ethanol ODH in a continuous flow tube reactor. First, the catalysts were pre-treated with the reaction mixture at 280 °C till steady-state behavior was reached (see Figure S1, supporting information). After this induction period of approximately 20 h isothermal catalytic experiments between 200 and 300 °C were carried out. The carbon mole balance during temperature cycling was 98.5–100%. The resulting degree of conversion of ethanol and the acetaldehyde selectivity are shown in Figure 1a and b. Besides the desired product acetaldehyde, formation of ethylene and CO was detected. Over two hours at 200 °C, p-$Fe_2(MoO_4)_3$ shows an increase in degree of conversion from 12 to 17%. For all other temperatures and both materials steady-state could be reached and stable degrees of conversion and selectivity were observed. The steady-state values of degree of conversion and selectivities to the reaction products are shown in Figure 1c and d. Below 280 °C, both catalysts show a high acetaldehyde selectivity of >95%. Only at high conversions ($X > 90$%) formation of ethylene and small amounts of CO_x are detected for p-$Fe_2(MoO_4)_3$. At 280 °C p-$Fe_2(MoO_4)_3$ shows an activity of 6.71 $\mathrm{mmol_{AcH}\,s^{-1}\,kg_{cat}^{-1}}$ and a degree of conversion of 93.5% with an acetaldehyde selectivity of 96.5% ($Y_{AcH} = 90.3$%).

The iron molybdate prepared by solid-state synthesis shows a lower activity. At 280 °C, an activity of 3.0 $\mathrm{mmol_{AcH}\,s^{-1}\,kg_{cat}^{-1}}$ is observed and the yield of acetaldehyde is 60.4% ($X_{EtOH} = 63$% and $S_{AcH} = 96$%). After increasing the temperature gradually to 280 °C, the temperature was lowered step by step to study a

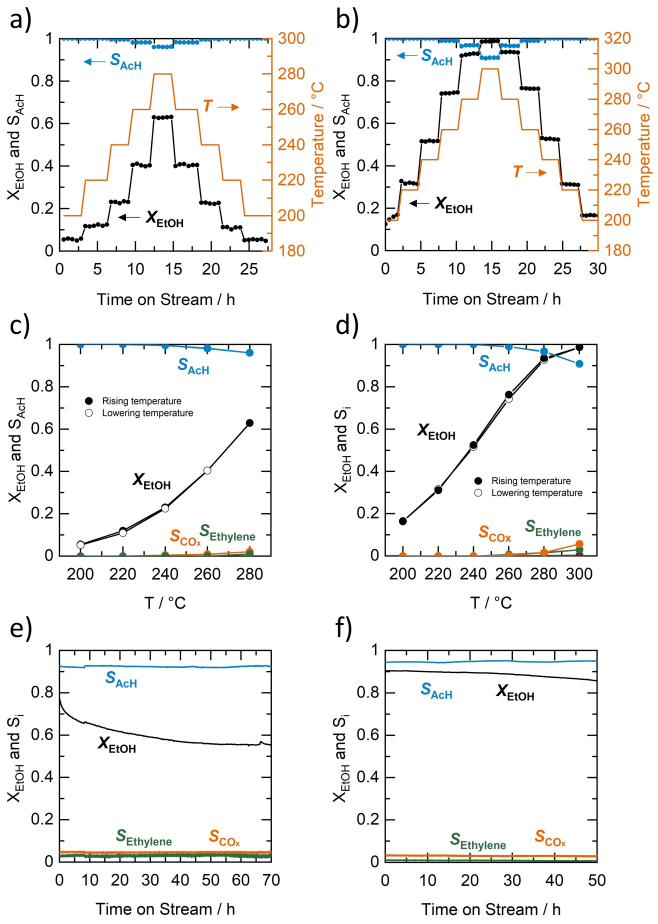

Figure 1. Conversion of ethanol (EtOH) and selectivity to acetaldehyde (AcH) during temperature variation against time on stream for a) 150 mg bm-$Fe_2(MoO_4)_3$ and b) 100 mg p-$Fe_2(MoO_4)_3$; Steady-state values for the conversion of ethanol and the selectivities to acetaldehyde, CO_x and ethylene against reaction temperature for c) 150 mg bm-$Fe_2(MoO_4)_3$ and d) 100 mg p-$Fe_2(MoO_4)_3$; Conversion of ethanol and selectivity to products at 280 °C for 70 h for e) 150 mg bm-$Fe_2(MoO_4)_3$ and f) 100 mg p-$Fe_2(MoO_4)_3$. Feed-flow characteristics in all measurements: 5 vol% EtOH, 10 vol% O_2, 85 vol% He, total volume flow: 20 $ml_{STP}\,min^{-1}$.

potential temperature hysteresis. The averaged steady-state values of the degree of conversion and the selectivities in Figure 1c and d show that for both materials no temperature hysteresis is observed (raising temperature: closed symbols, lowering temperature: open symbols). Figure 1e and f depict long-term measurements of both materials at 280 °C (including the described induction period). bm-$Fe_2(MoO_4)_3$ shows a decrease in the degree of conversion from 78% at the beginning to 56% after 70 h time on stream, while the acetaldehyde selectivity remains constant at 93%. For p-$Fe_2(MoO_4)_3$, starting at a degree of conversion of 93%, a slow decline to 86% is observed over 70 h. The selectivity to acetaldehyde is slightly increasing from 93 to 95%.

Methanol ODH. To compare the results of this study to literature findings, the activity and selectivity in the methanol ODH was also assessed since most work on ODH catalysis with iron molybdates was done with methanol as substrate. For methanol ODH, after reaching steady-state conditions at 300 °C, the temperature was varied within 240–340 °C. The carbon mole balance during temperature cycling was 98–100%. The time on stream resolved results are presented in Figure S3 and show a slight deactivation of the materials. Figure 2 depicts the conversion of methanol and the selectivities to the products after holding each temperature for 2 h. For both materials, besides the desired product formaldehyde, dimethoxymethane and dimethyl ether, as well as traces of carbon monoxide are detected. At temperatures below 240 °C, dimethoxymethane (DMM) is the main side product with selectivities of 10–20%. With increasing temperature, the formaldehyde selectivity increases, and dimethyl ether (DME) becomes the main side product. At 320 °C, p-$Fe_2(MoO_4)_3$ shows high formaldehyde yields of 84.7% at a degree of conversion of 87% with an activity of 12.6 $mmol_{FAld}\,s^{-1}\,kg_{cat}^{-1}$. The methanol ODH activity and selectivity of that catalyst is comparable to the literature data (320 °C: 6.7 $mmol_{FAld}\,s^{-1}\,kg_{cat}^{-1}$, X_{MeOH} = 91%, Y_{FAld} = 86%).[46] bm-$Fe_2(MoO_4)_3$ shows a lower activity and at 320 °C a degree of conversion of 56% (4.6 $mmol_{FAld}\,s^{-1}\,kg_{cat}^{-1}$). Different to p-$Fe_2(MoO_4)_3$, the DME selectivity does not drop at higher temperatures and ranges within 14–17%. Thus, for bm-$Fe_2(MoO_4)_3$ a lower formaldehyde yield of 45.9% results at 320 °C.

Catalyst Characterization. To study the morphology and texture of the synthesized materials, SEM images were taken and N_2-physisorption measurements were performed. SEM images of both materials prior and after catalytic testing are shown in Figure 3. The precipitated p-$Fe_2(MoO_4)_3$ consists of rough particles in the range of 2–8 µm. The morphology is preserved during ODH experiments. The ball-milled bm-$Fe_2(MoO_4)_3$ shows crushed particles which are predominantly <10 µm in size. The morphology of bm-$Fe_2(MoO_4)_3$ also seems to be unaltered after catalysis.

Nitrogen physisorption experiments reveal specific surface areas of 2.9 $m^2\,g^{-1}$ for p-$Fe_2(MoO_4)_3$ and 2.6 $m^2\,g^{-1}$ for bm-$Fe_2(MoO_4)_3$, which do not significantly change during the ODH experiments (spent p-$Fe_2(MoO_4)_3$: 2.8 $m^2\,g^{-1}$ and spent bm-$Fe_2(MoO4)_3$: 2.6 $m^2\,g^{-1}$).

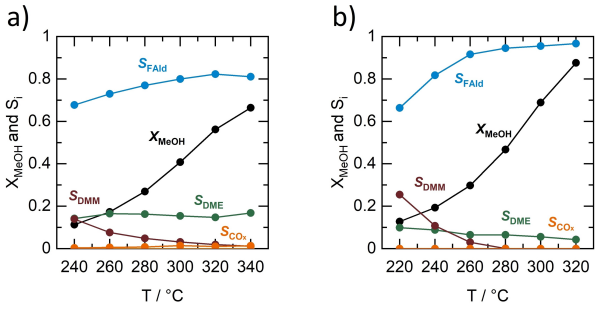

Figure 2. Conversion of methanol (MeOH) and selectivity to formaldehyde (FAld), dimethyl ether (DME), dimethoxymethane (DMM) and CO_x for different reaction temperatures for a) 100 mg bm-$Fe_2(MoO_4)_3$ and b) 100 mg p-$Fe_2(MoO_4)_3$. Feed-flow characteristics: 10 vol% MeOH, 10 vol% O_2, 80 vol% He, total volume flow: 20 $ml_{STP}\,min^{-1}$.

Table 1. Summary of elemental compositions measured by ICP-OES, SEM-EDX and XPS.

Sample	ICP-OES Mo/Fe	Stoichiometry	SEM-EDX Mo [at%]	Fe [at%]	O [at%]	Mo/Fe	Stoichiometry	XPS Fe [at%]	Mo [at%]	O [at%]	Mo/Fe
p-$Fe_2(MoO_4)_3$	1.53	$Fe_2Mo_{3.06}O_{12.09}$	17.0	11.4	71.7	1.50	$Fe_2Mo_{3.0}O_{12.5}$	4.5	15.8	61.4	3.51
Spent p-$Fe_2(MoO_4)_3$	1.55	$Fe_2Mo_{3.09}O_{13.04}$	14.6	9.5	75.9	1.53	$Fe_2Mo_{3.1}O_{15.9}$	4.2	13.6	60.1	3.24
bm-$Fe_2(MoO_4)_3$	1.48	$Fe_2Mo_{2.96}O_{12.19}$	17.2	12.2	70.5	1.41	$Fe_2Mo_{2.9}O_{11.5}$	4.8	15.0	59.1	3.13
Spent bm-$Fe_2(MoO_4)_3$	1.51	$Fe_2Mo_{3.02}O_{11.83}$	17.3	11.8	71.0	1.47	$Fe_2Mo_{2.9}O_{12.0}$	5.0	12.6	54.8	2.52

ICP-OES analysis of both materials was carried out to determine the composition of the materials. The atomic ratios of molybdenum and iron and the calculated stoichiometries of the pristine and spent materials are summarized in Table 1. The Mo/Fe ratio is detected to be close to 1.5 for all materials confirming the theoretical stoichiometry of $Fe_2(MoO_4)_3$. There is no significant change in the elemental composition observable after the catalytic tests.

The elemental composition is further confirmed by SEM/EDX. In the margin of error, the theoretical Mo/Fe ratio of 1.5 is verified for all samples prior and after catalytic testing. For the spent catalysts a slight increase in oxygen content can be observed.

X-ray photoelectron spectroscopy was performed to determine the surface composition of the catalysts and the resulting elemental compositions are summarized in Table 1. The pristine materials show a surface Mo/Fe ratio of 3.51 (p-$Fe_2(MoO_4)_3$) and 3.13 (bm-$Fe_2(MoO_4)_3$), which is significantly higher than the theoretical value of 1.5 determined with the bulk characterization methods. These higher Mo/Fe ratios indicate an enrichment of molybdenum on the catalyst surface. After ODH experiments the Mo/Fe ratios are slightly decreasing to 3.24 for p-$Fe_2(MoO_4)_3$ and more pronounced to 2.52 for bm-$Fe_3(MoO_4)_3$, respectively. Besides an enrichment of molybdenum, the oxygen content O/(Mo + Fe) measured by XPS is higher for p-$Fe_2(MoO_4)_3$ (3.02) and bm-$Fe_2(MoO_4)_3$ (2.98), as compared to the theoretical value of 2.4 for $Fe_2(MoO_4)_3$. During ethanol ODH, the O/(Mo + Fe) ratio is slightly increasing to 3.34 (p-$Fe_2(MoO_4)_3$) and 3.11 (bm-$Fe_2(MoO_4)_3$).

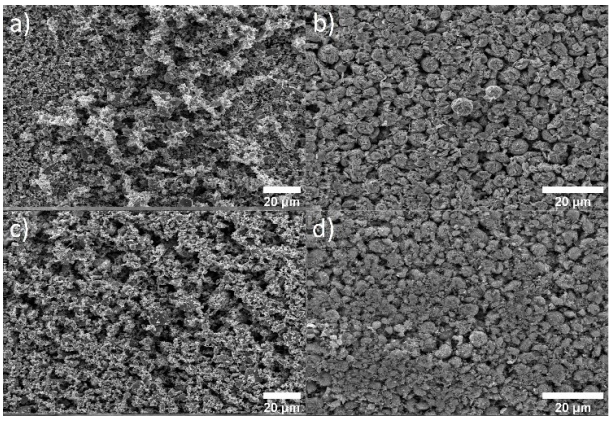

Figure 3. SEM images of iron molybdate samples: a) pristine bm-$Fe_2(MoO_4)_3$, b) pristine p-$Fe_2(MoO_4)_3$, c) spent bm-$Fe_2(MoO_4)_3$ and d) spent p-$Fe_2(MoO_4)_3$.

Raman spectroscopy was used for further characterization of the materials. The Raman spectra of the pristine and the spent catalysts are shown in Figure 4. The Raman bands can be assigned to bulk $Fe_2(MoO_4)_3$, in good agreement with literature data.[47,48] The triplet of bands between 930 and 1000 cm^{-1} is caused by MoO_4 symmetric and the bands at 785 and 823 cm^{-1} by MoO_4 antisymmetric stretching modes.[48] The Raman features around 350 cm^{-1} and within 117–258 cm^{-1} can be assigned to MoO_4 bending and lattice modes, respectively.[48] The spectra of the spent materials show the same Raman features as the pristine materials. In addition, a slight increase of the background is observed for the spent materials.

Mössbauer spectroscopy was employed to validate the oxidation state of iron in $Fe_2(MoO_4)_3$. Mössbauer spectra of the pristine and spent catalysts are shown Figure 5. Mössbauer hyperfine parameters are summarized Table 2 and indicate the iron to be in a +3 oxidation state (high spin) in agreement with literature data for phase pure $Fe_2(MoO_4)_3$.[49,50]

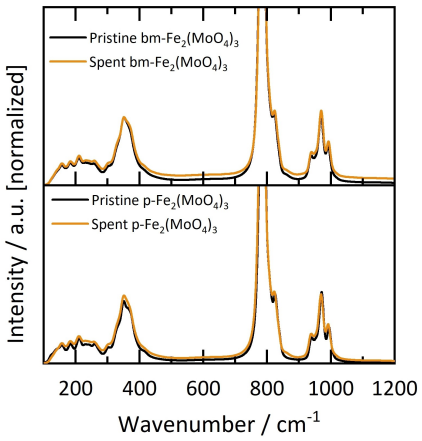

Figure 4. Raman spectra (514.5 nm) of pristine and spent iron molybdate samples; top: bm-$Fe_2(MoO_4)_3$ and bottom: p-$Fe_2(MoO_4)_3$.

Table 2. Mössbauer hyperfine parameters: Isomer shift (IS), quadrupole splitting (QS).

Sample	IS [mm s^{-1}]	QS [mm s^{-1}]	FWHM [mm s^{-1}]
p-$Fe_2(MoO_4)_3$	0.42	0.15	0.40
Spent p-$Fe_2(MoO_4)_3$	0.41	0.16	0.38
bm-$Fe_2(MoO_4)_3$	0.41	0.17	0.19
Spent bm-$Fe_2(MoO_4)_3$	0.41	0.19	0.17
Literature[49,50]	0.42–0.44	0.20–0.21	0.27–0.32
	0.42	0.18	0.27

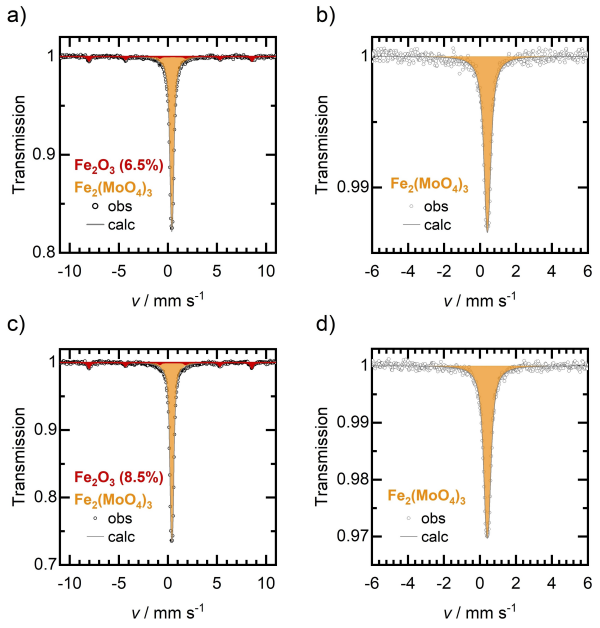

Figure 5. Mössbauer spectra of iron molybdate samples. a) bm-$Fe_2(MoO_4)_3$, b) p-$Fe_2(MoO_4)_3$, c) spent bm-$Fe_2(MoO_4)_3$ and d) spent p-$Fe_2(MoO_4)_3$.

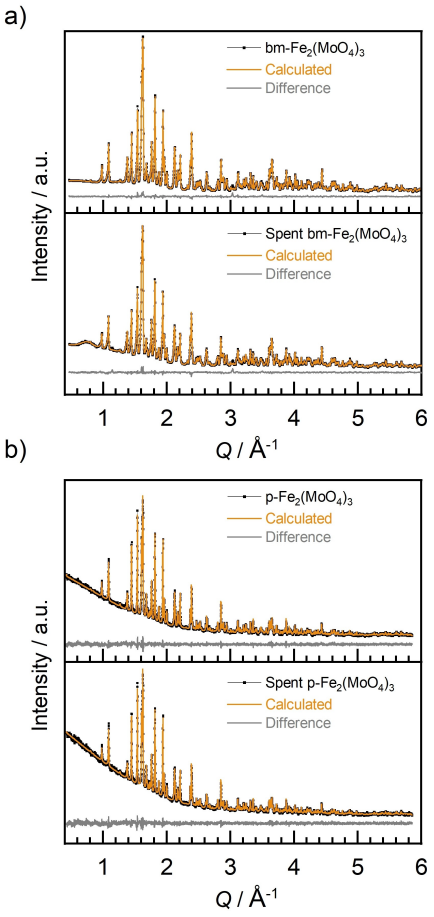

Figure 6. X-ray diffraction patterns and Rietveld refinements of a) pristine and spent bm-$Fe_2(MoO_4)_3$ and b) pristine and spent p-$Fe_2(MoO_4)_3$. (black: measured, orange: calculated, grey: difference curve).

In addition, Fe_2O_3 (hematite) is detected as an impurity in the bm-$Fe_2(MoO_4)_3$ samples and its amount is determined to be 6.5% in the pristine sample and 8.5% in the sample after catalytic testing. In contrast, the material prepared by precipitation shows no signs of Fe_2O_3 impurities neither prior nor after catalysis. The identical Mössbauer spectra of p-$Fe_2(MoO_4)_3$ before and after catalysis indicate its good structural stability and purity. The rather small values of quadrupole splitting indicate only minor distortions in FeO_6 octahedra.

The structure of $Fe_2(MoO_4)_3$ could be confirmed by Rietveld-refinement of the XRD powder data based on literature known structure model.[51] For bm-$Fe_2(MoO_4)_3$, the Fe_2O_3 impurity is determined to be less than 1.5 wt%. The results are shown in Figure 6.

Discussion

Regarding methanol ODH the precipitated catalyst shows a reactivity very similar to iron molybdate catalysts reported in literature.[46] It seems to be justified to draw parallels between the ethanol ODH studied in this work and the earlier investigated methanol ODH. Interestingly, in methanol ODH slight differences in activity and selectivity were observable between bm-$Fe_2(MoO_4)_3$ and p-$Fe_2(MoO_4)_3$. The formation of DME during methanol ODH is believed to take place on acidic sites. NH_3-TPD measurements are shown in Figure S6 and confirm a higher acidity of bm-$Fe_2(MoO_4)_3$. The total amount of desorbed NH_3 is determined to be 22.7 $mmol_{NH3}\,kg_{cat}^{-1}$ for bm-$Fe_2(MoO_4)_3$ and only 13.1 $mmol_{NH3}\,kg_{cat}^{-1}$ for p-$Fe_2(MoO_4)_3$. The higher overall acidity of bm-$Fe_2(MoO_4)_3$ could be the reason for the higher DME selectivity of this material. The origin of the higher acidity of bm-$Fe_2(MoO_4)_3$ could not be clarified yet.

The activity differences between both materials in the ODH of ethanol could originate from the different Mo/Fe ratios on the catalyst surface. While the elemental composition and the $Fe_2(MoO_4)_3$ structure was confirmed by ICP-OES, SEM/EDX, Raman spectroscopy and XRD for both materials, the XPS characterization proved a higher surface Mo/Fe ratio for the more active p-$Fe_2(MoO_4)_3$ (XPS: p-$Fe_2(MoO_4)_3$: Mo/Fe = 3.51, bm-$Fe_2(MoO_4)_3$: Mo/Fe = 3.13). This molybdenum enriched surface layer has been stated to be indispensable for an active and selective methanol ODH catalyst.[46,52] The lower Mo/Fe ratio of bm-$Fe_2(MoO_4)_3$ in comparison to p-$Fe_2(MoO_4)_3$ could offer an explanation for the lower activity in ethanol ODH and could originate from the high synthesis/calcination temperature (850 °C) of bm-$Fe_2(MoO_4)_3$. At this temperature, MoO_3 may evaporate from the catalyst surface leading to a lower Mo/Fe ratio compared to p-$Fe_2(MoO_4)_3$ calcined at 500 °C.

Regarding ethanol ODH an Y_{AcH}/X_{EtOH} diagram is given in Figure S4. It shows that the selectivity of bm-$Fe_2(MoO_4)_3$ is lower than that of the material synthesized by precipitation, but the differences are minor compared to methanol ODH. The reason

for the slightly lower selectivity is expected to be the same as in methanol ODH. The acidic catalyst side reaction in ethanol ODH is the ethylene production, which is nevertheless less pronounced compared to the DME pathway in methanol ODH. Thus, the selectivity drop in ethanol ODH is lower and both materials show high selectivities to acetaldehyde.

Activity differences between the two materials are clearly observable for both reactions. These seem not to originate from different specific surface areas but rather the overall lower surface Mo/Fe ratio of bm-$Fe_2(MoO_4)_3$, which shows that less MoO_x is exposed for the solid-state synthesis stemming material.

In ethanol ODH no catalyst deactivation is observable during temperature cycling (30 h time on stream). While most of the bulk characterization techniques showed no reaction-induced changes, especially the surface sensitive XPS measurements revealed a drop of the Mo/Fe ratio for both catalyst systems. This surface depletion of molybdenum could be a first indication for long-term deactivation of the catalyst. From methanol ODH it is known, that MoO_x from the catalyst may sublimate leading to a deactivation of the catalyst. Molybdenum-oxy-methoxy or molybdenum–oxy-hydroxy species are formed from surface MoO_3 under reaction conditions and are believed to be the volatile compounds that lead to a loss of molybdenum.[37–40] Interestingly, Mössbauer spectroscopy also showed an enrichment of Fe_2O_3 during testing, which is a second indication for a slight molybdenum loss during the stability testing. It seems, that in ethanol ODH a similar deactivation mechanism applies as for the methanol ODH. Nevertheless, for steady-state experiments with 70 h time on stream at 280 °C (including the induction period) a deactivation is observable (bm-$Fe_2(MoO_4)_3$: from 3.56 to 2.55 $mmol_{AcH}\,s^{-1}\,kg_{cat}^{-1}$; p-$Fe_2(MoO_4)_3$ from 6.43 to 6.07 $mmol_{AcH}\,s^{-1}\,kg_{cat}^{-1}$) supporting the described assumptions concerning catalyst deactivation. Nevertheless, more detailed studies are necessary to corroborate these initial findings.

Conclusion

Two stoichiometric iron molybdate catalysts, one prepared by co-precipitation and one synthesized by a ball-milled solid-state reaction route, were applied as catalysts in the ODH of ethanol. Both materials show attractive activity and selectivity towards acetaldehyde and a stable performance under the conditions applied in this study. The catalyst synthesized by the solid-state method is slightly less active and selective than the precipitated one. The higher acidity and lower Mo content on the catalyst surface are proposed to be the reason for the lower activity and selectivity. Further approaches based on this modified synthesis method could be attractive especially in terms of controlling the Fe_2O_3 content and the Mo/Fe ratio on the catalyst surface and the impact on ODH activity and selectivity.

Similar to previous observations for methanol ODH, a depletion of surface molybdenum during ethanol ODH could be observed for both catalysts. Further studies on catalyst long-term stability and stability under higher temperatures and ethanol concentrations together with extensive ex-situ and in-situ characterization need to be carried out in the future to deepen the insights on a possible long-term deactivation.

Experimental Section

Catalyst Preparation

Solid-State Synthesis. bm-$Fe_2(MoO_4)_3$ was synthesized from Fe_2O_3 (*Chempur*, 99.9%) and MoO_3 (*Chempur*, >99.9%) powders (stoichiometric ratio 1:3). The powders where mixed with acetone (*Fisher Chemicals*, ≥99.8%) and ball-milled for 15 minutes at 650 rpm in corundum crucibles using 9 corundum balls for batches between 10 to 15 g (Retsch PM 100 ball mill). After drying the ball-milled sample for at least 12 h, the mixture was transferred to a corundum crucible and then heated in a box furnace under ambient atmosphere up to 850 °C (200 °C h^{-1}, hold: 15 h). After cooling to room temperature, the material was ball milled twice for 10 and 15 minutes at 650 rpm.

Precipitation. p-$Fe_2(MoO_4)_3$ was prepared using a co-precipitation synthesis procedure according to ref. [49] Iron nitrate nonahydrate (14.9 mmol, $Fe(NO_3)_3 \cdot 9\ H_2O$, *Merck*, ≥98%) and ammonium heptamolybdate tetrahydrate (22.3 mmol, $(NH_4)_6Mo_7O_{24} \cdot 7\ H_2O$, *Merck*, ≥99%) were dissolved separately in demineralized water (100 resp. 200 mL). Afterwards, the aqueous iron nitrate solution was added dropwise to the molybdate solution under vigorous stirring, which instantly led to the formation of a precipitate. In order to complete the precipitation process, the solution was stirred at 100 °C for three more hours. The precipitate was isolated by filtering off and washed with demineralized water and ethanol (*Brentag BCD*, Technical Grade) before it was dried overnight at 100 °C in air. Finally, the powder was calcined in air at 500 °C for 10 h, using a corundum crucible and a tube furnace (Carbolite Gero CWF1200).

Catalyst Characterization

Vis-Raman Spectroscopy. Vis-Raman spectroscopy was performed at an excitation wavelength of 514.5 nm using an argon ion gas laser (Melles Griot). The light was focused onto the sample, gathered by an optic fibre and dispersed by a transmission spectrometer (Kaiser Optical, HL5R). The dispersed Raman radiation was subsequently detected by an electronically cooled CCD detector (−40 °C, 1024×256 pixels). The spectral resolution was 5 cm^{-1} with a wavelength stability of better than 0.5 cm^{-1}. A laser power of 4 mW at the sample location was applied. Data analysis of the Raman spectra included a cosmic ray removal and an auto new dark correction.

X-ray Photoelectron Spectroscopy. X-ray photo-electron spectroscopy (XPS) was carried out on an SSX 100 ESCA spectrometer (Surface Science Laboratories Inc.) employing a monochromatic Al K_α X-ray source (1486.6 eV) operated at 9 kV and 10 mA; the spot size was approximately 1 mm×0.25 mm. The base pressure of the analysis chamber was $<10^{-8}$ Torr. Survey spectra (eight measurements) were recorded between 0 and 1100 eV with 0.5 eV resolution, whereas detailed spectra (30 measurements) were recorded with 0.05 eV resolution. To account for sample charging, the C 1s peak of ubiquitous carbon at 284.4 eV was used to correct the binding-energy shifts in the spectra. Atomic concentrations were calculated using the relative sensitivity factors (RSFs) given in Table 3.

Table 3. Relative sensitivity factors used for the calculation of elemental concentrations from XPS data.

	C 1s	O 1s	Mo 3d	Fe $2p_{3/2}$	Si 2p
RSF	1.00	2.50	9.79	7.96	0.90

^{57}Fe Mössbauer Spectroscopy. The spectra of bm-$Fe_2(MoO_4)_3$ were acquired in transmission mode with a custom build setup at 294 K. An α-Fe foil was used for the calibration of the velocity. Mössbauer spectra of p-$Fe_2(MoO_4)_3$ were acquired in a custom build setup having a ^{57}Co/Rh radiation source equipped with a proportional counter. Velocity values are referenced to an α-Fe foil. The spectra were fitted by Lorentzian Lineshape Analysis using the software *Recoil*.[53]

SEM/EDX. Scanning electron microscopy (Philips XL30 FEG, 20 kV) and energy-dispersive spectroscopy (EDAX Si detector, liquid nitrogen-cooled) was used to check for homogeneity, particle size and composition. Small amounts (~3 mg) of finely ground powder were transferred onto a double-sided carbon tape fixed on an aluminium specimen holder.

X-ray powder diffraction. X-ray powder diffraction of bm-$Fe_2(MoO_4)_3$ was performed using a Stoe STADI P diffractometer with Mo $K_{\alpha1}$ radiation in transmission mode. Rietveld refinements were performed using the software TOPAS.[54]

p-$Fe_2(MoO_4)_3$ was analysed in transmission geometry (Stoe & Cie GmbH, StadiP, Cu $K_{\alpha1}$ radiation, Ge(111) monochromator, Dectris/Mythen 1 K). Small amounts of the powder samples were placed on acetate foil. Rietveld refinements were performed using the software TOPAS.[54]

ICP-OES. Inductive coupled plasma optical emission spectrometry (ICP-OES) was carried out using a PerkinElmer OPTIMA 2000DV spectrometer. For sample preparation the materials were dissolved in aqua regia and diluted with deionized water.

N_2-Physisorption. Physisorption measurements were carried out using the volumetric measuring system Quadrasorb evo from Quantachrome GmbH & Co. KG (Odelzhausen, Germany). Specific surface areas were calculated using the MBET method.

Catalytic Measurements

The catalytic reactions were performed in a continuous flow apparatus with quartz glass tube reactor with an internal diameter of 4 mm (see Scheme S1). The catalyst was placed between two glass wool plugs. Liquid reactants (methanol >99.95%, *Carl Roth* and ethanol >99%, *Fisher Scientific*) were fed to the reactor by using a saturator system and gases (Helium 5.0, *Westfalen*; Oxygen 4.8, *Air Liquid*) were dosed by mass flow controllers. The total volume flow was 20 ml min^{-1} (STP) with helium as inert gas. Off-gas analytic was performed by an online quadrupole mass spectrometer (GAM 400, InProcess Instruments) and an online gas chromatograph (Shimadzu GC 2010) equipped with a FID and a TCD detector.

Methanol ODH. For the methanol ODH reference measurements, the feed consisted of 10 vol% methanol and 10 vol% O_2. 100 mg of catalyst were used and pre-treated with the reaction mixture at 320 °C until steady state conditions were reached. Afterwards the temperature was varied within 220–320 °C in steps of 20 K. The spent catalyst corresponds to the material after the temperature variation.

Ethanol ODH. For the ethanol ODH measurements, the feed consisted of 5 vol% ethanol and 10 vol% O_2. 100 mg p-$Fe_2(MoO_4)_3$ and 150 mg bm-$Fe_2(MoO_4)_3$ were used and pre-treated with the reaction mixture at 280 °C until steady-state conditions were reached. Afterwards the temperature was varied within 200–280 °C in steps of 20 K. The spent catalyst corresponds to the material after the temperature variation. For the long-term measurements, the as prepared catalysts (p-$Fe_2(MoO_4)_3$: 100 mg; bm-$Fe_2(MoO_4)_3$: 150 mg) were heated to 280 °C and stationary measurements were performed for 70 h.

All data can be found via TUDatalib (DOIs and links in supporting information).

Acknowledgements

The authors gratefully acknowledge financial support from Technische Universität Darmstadt and Johannes Gutenberg-Universität Mainz. The authors also thank Vasily Potapkin, Vadim Ksenofontov, Kathrin Hofmann, Patrick Schmatz-Engert and Alfons Drochner for their help within this study, as well as Karl Kopp for performing the XPS experiments and the research group of Prof. Rose for performing the NH_3-TPD measurements. Open Access funding enabled and organized by Projekt DEAL.

Conflict of Interest

The authors declare no conflict of interest.

Keywords: acetaldehyde · dehydrogenation · ethanol · heterogeneous catalysis · iron molybdate

[1] M. Carus, F. Kähler, O. Porc, "Global Carbon Demand for Chemicals and Derived Materials," **2021**.
[2] P. Bajpai, *Developments in Bioethanol*, Springer Singapore, Singapore, **2021**.
[3] FAO, OECD, *OECD-FAO Agric. Outlook* **2015**, 145.
[4] A. Mohsenzadeh, A. Zamani, M. J. Taherzadeh, *ChemBioEng Rev.* **2017**, *4*, 75–91.
[5] M. Cozzolino, R. Tesser, M. Di Serio, P. D'Onofrio, E. Santacesaria, *Catal. Today* **2007**, *128*, 191–200.
[6] M. Eckert, G. Fleischmann, R. Jira, H. M. Bolt, K. Golka, *Ullmann's Encyclopedia of Industrial Chemistry*, Wiley-VCH Verlag GmbH & Co. KGaA., Weinheim, **2006**.
[7] T. V. Andrushkevich, V. V. Kaichev, Y. A. Chesalov, A. A. Saraev, V. I. Buktiyarov, *Catal. Today* **2017**, *279*, 95–106.
[8] R. Bulánek, P. Čičmanec, J. Kotera, I. Boldog, *Catal. Today* **2019**, *324*, 106–114.
[9] B. Kilos, A. T. Bell, E. Iglesia, *J. Phys. Chem. C* **2009**, *113*, 2830–2836.
[10] R. Tesser, V. Maradei, M. Di Serio, E. Santacesaria, *Ind. Eng. Chem. Res.* **2004**, *43*, 1623–1633.
[11] E. Santacesaria, A. Sorrentino, R. Tesser, M. Di Serio, A. Ruggiero, *J. Mol. Catal. A* **2003**, *204–205*, 617–627.
[12] J. L. Lakshmi, N. J. Ihasz, J. M. Miller, *J. Mol. Catal. A* **2001**, *165*, 199–209.
[13] V. I. Sobolev, E. V. Danilevich, K. Y. Koltunov, *Kinet. Catal.* **2013**, *54*, 730–734.
[14] P. Ober, S. Rogg, C. Hess, *ACS Catal.* **2020**, *10*, 2999–3008.
[15] P. Waleska, S. Rupp, C. Hess, *J. Phys. Chem. C* **2018**, *122*, 3386–3400.
[16] P. Waleska, C. Hess, *Catal. Lett.* **2018**, *148*, 2537–2547.
[17] P. Čičmanec, Y. Ganjkhanlou, J. Kotera, J. M. Hidalgo, Z. Tišler, R. Bulánek, *Appl. Catal. A* **2018**, *564*, 208–217.
[18] J. M. Hidalgo-Herrador, Z. Tišler, *Period. Polytech. Chem. Eng.* **2018**, *62*, 345–350.

[19] I. Boldog, P. Čičmanec, Y. Ganjkhanlou, R. Bulánek, *Catal. Today* **2018**, *304*, 64–71.
[20] Y. Ganjkhanlou, Z. Tišler, J. M. Hidalgo, K. Frolich, J. Kotera, P. Čičmanec, R. Bulánek, *Chem. Pap.* **2018**, *72*, 937–946.
[21] J. M. Hidalgo, Z. Tišler, D. Kubička, K. Raabova, R. Bulanek, *J. Mol. Catal. A* **2016**, *420*, 178–189.
[22] V. V. Kaichev, Y. A. Chesalov, A. A. Saraev, A. Y. Klyushin, A. Knop-Gericke, T. V. Andrushkevich, V. I. Bukhtiyarov, *J. Catal.* **2016**, *338*, 82–93.
[23] B. Beck, M. Harth, N. G. Hamilton, C. Carrero, J. J. Uhlrich, A. Trunschke, S. Shaikhutdinov, H. Schubert, H. J. Freund, R. Schlögl, J. Sauer, R. Schomäcker, *J. Catal.* **2012**, *296*, 120–131.
[24] H. Nair, J. E. Gatt, J. T. Miller, C. D. Baertsch, *J. Catal.* **2011**, *279*, 144–154.
[25] A. Malmusi, J. Velasquez Ochoa, T. Tabanelli, F. Basile, C. Lucarelli, S. Agnoli, F. Carraro, G. Granozzi, F. Cavani, *Appl. Catal. A* **2019**, *570*, 139–147.
[26] V. I. Sobolev, K. Y. Koltunov, *ChemCatChem* **2011**, *3*, 1143–1145.
[27] G. V. Mamontov, M. V. Grabchenko, V. I. Sobolev, V. I. Zaikovskii, O. V. Vodyankina, *Appl. Catal. A* **2016**, *528*, 161–167.
[28] V. V. Dutov, G. V. Mamontov, V. I. Sobolev, O. V. Vodyankina, *Catal. Today* **2016**, *278*, 164–173.
[29] A. S. Blokhina, I. A. Kurzina, V. I. Sobolev, K. Y. Koltunov, G. V. Mamontov, O. V. Vodyankina, *Kinet. Catal.* **2012**, *53*, 477–481.
[30] P. Liu, E. J. M. Hensen, *J. Am. Chem. Soc.* **2013**, *135*, 14032–14035.
[31] F. Herold, S. Prosch, N. Oefner, K. Brunnengräber, O. Leubner, Y. Hermans, K. Hofmann, A. Drochner, J. P. Hofmann, W. Qi, B. J. M. Etzold, *Angew. Chem. Int. Ed.* **2021**, *60*, 5898–5906; *Angew. Chem.* **2021**, *133*, 5962–5971.
[32] R. D. Weinstein, A. R. Ferens, R. J. Orange, P. Lemaire, *Carbon N. Y.* **2011**, *49*, 701–707.
[33] I. Abdullahi, T. J. Davis, D. M. Yun, J. E. Herrera, *Appl. Catal. A* **2014**, *469*, 8–17.
[34] A. W. Franz, H. Kronemayer, D. Pfeiffer, R. D. Pilz, G. Reuss, W. Disteldorf, A. O. Gamer, A. Hilt, *Ullmann's Encyclopedia of Industrial Chemistry*, Wiley-VCH Verlag GmbH & Co. KGaA, Weinheim, **2016**.
[35] A. P. Vieira Soares, M. Farinha Portela, A. Kiennemann, *Catal. Rev. Sci. Eng.* **2005**, *47*, 125–174.
[36] C. Brookes, M. Bowker, P. P. Wells, *Catalysts* **2016**, *6*, 92–118.
[37] K. I. Ivanov, D. Y. Dimitrov, *Catal. Today* **2010**, *154*, 250–255.
[38] A. Andersson, M. Hernelind, O. Augustsson, *Catal. Today* **2006**, *112*, 40–44.
[39] A. Gaur, M. Stehle, K. V. Raun, J. Thrane, A. D. Jensen, J. D. Grunwaldt, M. Høj, *Phys. Chem. Chem. Phys.* **2020**, *22*, 11713–11723.
[40] A. Gaur, M. Schumann, K. V. Raun, M. Stehle, P. Beato, A. D. Jensen, J. D. Grunwaldt, M. Høj, *ChemCatChem* **2019**, *11*, 4871–4883.
[41] K. V. Raun, J. Johannessen, K. McCormack, C. C. Appel, S. Baier, M. Thorhauge, M. Høj, A. D. Jensen, *Chem. Eng. J.* **2019**, *361*, 1285–1295.
[42] J. E. Gatt, H. Nair, C. D. Baertsch, *Appl. Catal. B* **2010**, *99*, 127–134.
[43] Y. L. Xiong, R. Castillo, C. Papadopoulou, L. Daza, J. Ladrière, P. Ruiz, B. Delmon, *Stud. Surf. Sci. Catal.* **1991**, *68*, 425–432.
[44] K. A. Thavornprasert, B. De La Goublaye De Ménorval, M. Capron, J. Gornay, L. Jalowiecki-Duhamel, X. Sécordel, S. Cristol, J. L. Dubois, F. Dumeignil, *Biofuels* **2012**, *3*, 25–34.
[45] V. Srihari, D. S. Viswanath, *J. Chem. Technol. Biotechnol.* **1982**, *32*, 868–876.
[46] B. R. Yeo, G. J. F. Pudge, K. G. Bugler, A. V. Rushby, S. Kondrat, J. Bartley, S. Golunski, S. H. Taylor, E. Gibson, P. P. Wells, C. Brookes, M. Bowker, G. J. Hutchings, *Surf. Sci.* **2016**, *648*, 163–169.
[47] H. Tian, I. E. Wachs, L. E. Briand, *J. Phys. Chem. B* **2005**, *109*, 23491–23499.
[48] J. Sejkora, J. Čejka, R. Malíková, A. López, Y. Xi, R. L. Frost, *Spectrochim. Acta Part A* **2014**, *130*, 83–89.
[49] A. P. V. Soares, M. F. Portela, A. Kiennemann, *Catal. Commun.* **2001**, *2*, 159–164.
[50] P. D. Battle, A. K. Cheetham, G. J. Long, G. Longworth, *Inorg. Chem.* **1982**, *21*, 4223–4228.
[51] H.-Y. Cheng, *Mater. Res. Bull.* **1979**, *14*, 1583–1590.
[52] S. Zhang, M. Han, *Molecules* **2020**, *25*, 2410–2420.
[53] K. Lagarec and D.G. Rancourt, Recoil, **1998**.
[54] TOPAS-Academic V6 Brisbane, Australie, **2016** .

Manuscript received: August 17, 2021
Revised manuscript received: October 29, 2021
Accepted manuscript online: December 13, 2021
Version of record online: January 12, 2022